The Company of **Biologists**

TECHNIQUES AND RESOURCES ARTICLE

A process engineering approach to increase organoid yield

Natasha Arora[1,*], Jasmin Imran Alsous[2,*], Jacob W. Guggenheim[3,*], Michael Mak[3], Jorge Munera[4], James M. Wells[4], Roger D. Kamm[1,3], H. Harry Asada[3], Stanislav Y. Shvartsman[2] and Linda G. Griffith[1,3,‡]

ABSTRACT

Temporal manipulation of the *in vitro* environment and growth factors can direct differentiation of human pluripotent stem cells into organoids – aggregates with multiple tissue-specific cell types and three-dimensional structure mimicking native organs. A mechanistic understanding of early organoid formation is essential for improving the robustness of these methods, which is necessary prior to use in drug development and regenerative medicine. We investigated intestinal organoid emergence, focusing on measurable parameters of hindgut spheroids, the intermediate step between definitive endoderm and mature organoids. We found that 13% of spheroids were pre-organoids that matured into intestinal organoids. Spheroids varied by several structural parameters: cell number, diameter and morphology. Hypothesizing that diameter and the morphological feature of an inner mass were key parameters for spheroid maturation, we sorted spheroids using an automated micropipette aspiration and release system and monitored the cultures for organoid formation. We discovered that populations of spheroids with a diameter greater than 75 µm and an inner mass are enriched 1.5- and 3.8-fold for pre-organoids, respectively, thus providing rational guidelines towards establishing a robust protocol for high quality intestinal organoids.

KEY WORDS: Organoids, Yield, Process engineering, Intestinal, Aggregates, Sorting

INTRODUCTION

Human pluripotent stem cells (hPSCs) can differentiate into any individual cell type, as well as into multicellular organoids that resemble kidney, brain, liver, stomach and intestine (Lancaster et al., 2013; Spence et al., 2011; Takasato et al., 2014; McCracken et al., 2014; Takebe et al., 2013; Lancaster and Knoblich, 2014). In the case of intestinal organoids, multiple tissue-specific cells deriving from both endodermal and mesodermal lineages self-assemble into a structure that mimics the epithelial lumen and surrounding tissue of the intestine (Spence et al., 2011). Because organoid formation requires the concerted differentiation and morphogenesis of multiple interacting cell types, the process is inherently difficult to understand and control, resulting in heterogeneous outcomes with

[1]Department of Biological Engineering, Massachusetts Institute of Technology, 77 Massachusetts Ave, Cambridge, MA 02139, USA. [2]Department of Chemical and Biological Engineering, Princeton University, Washington Road, Princeton, NJ 08540, USA. [3]Department of Mechanical Engineering, Massachusetts Institute of Technology, 77 Massachusetts Ave, Cambridge, MA 02139, USA. [4]Division of Developmental Biology, Cincinnati Children's Hospital Medical Center, 3333 Burnet Avenue, Cincinnati, OH 45229, USA.

*These authors contributed equally to this work

‡Author for correspondence (griff@mit.edu)

L.G.G., 0000-0002-1801-5548

low yields of viable organoids (Si-Tayeb et al., 2010; Świerczek et al., 2015; Tian et al., 2016; Yang et al., 2016; Zahabi et al., 2012; Zhang et al., 2012; Matthys et al., 2016; Purpura et al., 2012). Such inefficiencies hinder technological applications including disease modeling and drug development assays.

In development, communicating layers of endoderm and mesoderm give rise to the gut tube, which is the precursor to most respiratory and gastrointestinal organs (McDonald and Rossant, 2014; Rubin, 2007). *In vitro*, hindgut cultures comprising layers of posterior endoderm and mesoderm bud, then shed a heterogeneous population of spheroids with potential to form gut organoids when shifted to a conducive environment (Spence et al., 2011; Sun et al., 2002; Zhao et al., 2001; Sinagoga and Wells, 2015; Liu et al., 2015; Matano et al., 2015). For yet inexplicable reasons, only a small fraction of the regions that bud and form spheroids mature into organoids (McCracken et al., 2011); we refer here to such spheroids as 'pre-organoids'. If it were possible to use non-invasive metrics (e.g. *in situ* imaging) to predict which spheroids are pre-organoids, then the early stages of culture could be efficiently engineered, possibly bypassing the initial morphogenesis events, to produce a higher yield of desirable pre-organoids and thus organoids. Such improvement is essential to making organoid platforms tractable for large-scale studies and commercial applications such as pharmacogenomic profiling, selecting hits from drug screens, and optimizing lead compounds (Boehnke et al., 2016; Gordon et al., 2015; Edmondson et al., 2014; Eglen and Randle, 2015). Increasing the efficiency of pre-organoid production increases the predictability of downstream studies and decreases their scale while reducing costs and wasted reagents.

Here, we took a process engineering approach to improve the intestinal pre-organoid yield from hPSC-derived hindgut cultures. We identified morphological features that distinguish pre-organoids from spheroids. The intestinal organoid system was selected for this study because of its relative reproducibility and for the possibility of manipulating it systematically at various stages in the protocol.

RESULTS
Spheroid and hindgut heterogeneity

Spheroids obtained from our hindgut cultures resembled those of previous reports and had a similar prevalence of emergence (Spence et al., 2011). These 3D cell aggregates were easily visualized using nuclear marker DAPI (Fig. 1A). Spheroids displayed marked heterogeneity in diameter (defined in the Classification section of the Materials and Methods), in cell number, in cell type composition (epithelial and/or mesenchymal), and in the spatial organization of these cell types (Fig. 1B). We quantified the heterogeneity in these parameters to determine how and whether any of them predispose the spheroids to successful maturation into intestinal organoids (i.e. which spheroids are pre-organoids).

Spheroids began emerging from hindgut cultures 5 days after hindgut induction and continued budding for up to one additional week. We analyzed spheroids that budded on day 5 (D5), day 6
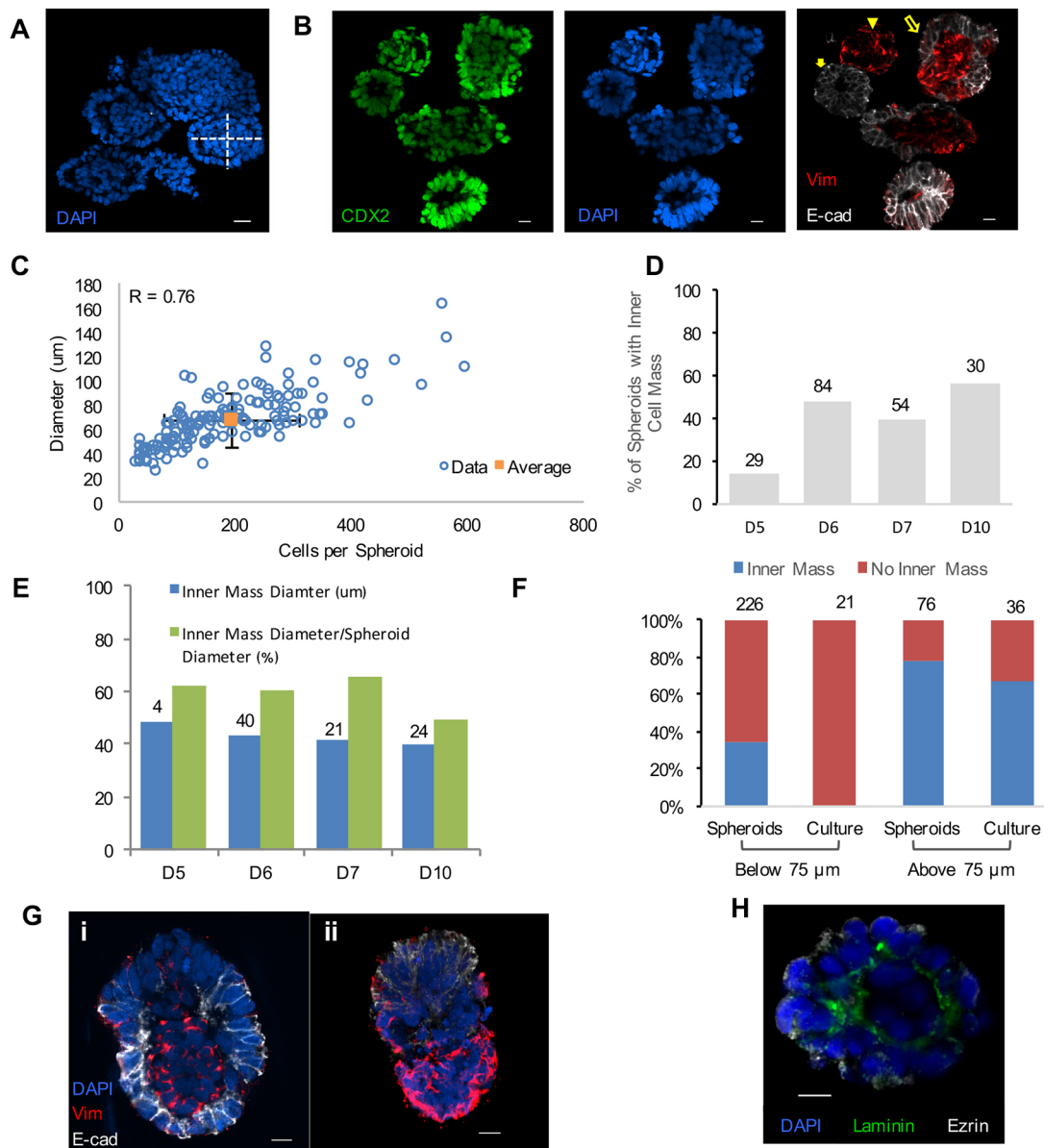
DEVELOPMENT

Fig. 1. Hindgut spheroid characterization. (A) DAPI staining allows visualization of spheroids. White dashed cross shows major and minor axes used to obtain an estimate for the diameter of a spheroid, which is an average of the major and minor axes. (B) Whole spheroids stain positive for hindgut marker CDX2 (green), whereas subpopulations stain for epithelial marker E-cadherin (white) and mesenchymal marker vimentin (red). Solid arrow: entirely epithelial; arrowhead: entirely mesenchymal; hollow arrow: inner mesenchyme, outer epithelial. (C) Scatter plots of spheroid diameter (µm) versus the number of cells per spheroid. Standard deviation is indicated. (D) Percentage of spheroids with an inner cell mass from time points during hindgut induction. The number on top of each bar indicates the number of spheroids analyzed. (E) Average diameter of the inner mass (blue) and the size of the inner mass relative to the spheroid (green). The number on top of each bar indicates the number of spheroids analyzed. (F) Percentage of all analyzed spheroids and buds in hindgut cultures that did or did not display the morphology of an inner mass with an outer ring, separated based on a threshold of a 75 µm diameter. The number on top of each bar indicates the number of spheroids analyzed. (G) Staining of spheroids for E-cadherin (white) and vimentin (red) allows for visualization of spatial organization of the cells. 3D renderings. (H) Polarized of epithelial cells was visualized with stains for apical marker ezrin (white) and basal marker laminin (green). Scale bars: 10 µm in A,B,G; 5 µm in H.

(D6), day 7 (D7) and day 10 (D10). There was variability in all metrics between experiments and cell lines. The data presented are reflective of the collective data across multiple experiments and two cell lines. Whereas all data shown are from hiPS72_3-derived spheroids, similar results were seen from H1.

Spheroid size (cell number and diameter)

Across all analyzed spheroids, the average number of cells per spheroid and the average diameter were (mean±s.d.) 193±117 cells and 68±22 µm, respectively (Fig. 1C). Although these parameters

are positively correlated (R=0.76), a comparison of the coefficient of variation for both parameters (0.60 and 0.32, respectively) shows greater variability in the number of cells per spheroid than in diameter (Fig. S2A,B).

Spatial organization and cell type composition

Spheroids displayed marked heterogeneity in cellular spatial organization, appearing as either homogenous cell aggregates or as a combination of two spatially segregated cell populations: an outer ring and an inner cell mass (Fig. 1B). Across all collection

days, 46% of spheroids had an inner mass. The spatial organization of a spheroid could be assessed through DAPI staining alone. The presence of an inner mass, however, varied across days, with D5 and D10 spheroids displaying the lowest and highest percentages thereof, respectively: 14% in D5, 48% in D6, 38% in D7 and 56% in D10 (Fig. 1D). Furthermore, the diameter of the inner mass ranged from 49.2% to 65.6% of the spheroid's diameter in D10 and D7 spheroids, respectively (Fig. 1E) and correlated positively with spheroid diameter (Fig. S2C). Measurements of the diameter of the inner mass relative to the spheroid's diameter are thus a proxy for the mesenchymal composition of a spheroid. Our data show no significant differences in that metric across all spheroids analyzed (Fig. 1E).

We also observed that spheroids greater than 75 µm in diameter were more likely to have an inner cell mass (Fig. 1F). Specifically, 34% versus 78% of spheroids below and above 75 µm, respectively, displayed the morphology of an inner mass with an outer ring. This suggests that formation of an inner mass in spheroids is mechanistically related, in as-yet-unknown ways, to a size threshold. In subsequent sections, we assessed the potential of spheroids greater than and less than 75 µm to mature into organoids.

To determine the cell-type composition of the spheroids, we stained the spheroids with mesenchymal (vimentin) and epithelial (E-cadherin) markers. Spheroids with a clearly delineated inner mass were composed of an outer ring of polarized epithelial cells enclosing mesenchymal cells clustered in the inner mass (Fig. 1Gi,H). Spheroids without an outer ring and inner mass contained either epithelial cells alone, mesenchymal cells alone, or, on rare occasions, both cell types separated spatially in a non-radial pattern (Fig. 1B,Gii). In the Discussion, we put forth a model for spheroid emergence from hindgut cultures that is consistent with and accounts for the observed heterogeneity in cell type composition in budding spheroids.

Heterogeneity across hindgut cultures

The heterogeneity of the size, cell composition and cell spatial organization of the budded spheroids arises from similar heterogeneity in the hindgut cultures. The hindgut cultures evolve from a monolayer of definitive endoderm into 3D, multi-layered, mixed cultures of endodermal epithelial and mesodermal cells (Fig. 2A,B). The global morphology in a relatively large region (1.2 mm×1.2 mm) of the culture revealed by staining that F-actin is characterized by heterogeneous bulges ranging from a few tens of microns up to a few hundred microns in diameter (Fig. 2A). Accumulations of cells positive for the epithelial marker E-cadherin appear scattered throughout the culture and largely separate from nests of cells expressing the mesenchymal marker vimentin (Fig. 2B). A nascent bud and the surrounding culture region stained for the extracellular matrix (ECM) protein laminin shows that laminin seems to accumulate in the central inner mass region of the bud (Fig. 2C,Ci), whereas cells expressing the epithelial cytoplasmic membrane protein ezrin appear localized to the exterior surface of the bud (Fig. 2C,Cii). The ECM protein fibronectin is excluded from the inner mass and seems to be localized between the laminin-rich inner mass and the outer ring of ezrin-expressing cells (Fig. 2D). Collagen IV is similarly excluded from the inner mass (Fig. 2D).

During differentiation, the hindgut cultures develop budding regions that seem to give rise to free-floating nascent spheroids. The diameter of the budding regions in the cultures is 97.6±43 µm. Of those regions, 41% have a clearly delineated inner mass and outer ring of cells (Fig. 1F). Budding regions do not seem to be uniformly interspersed; it remains unclear what causes certain regions of the culture to bud off as cell aggregates.

Automated spheroid sorting system

To test the hypothesis that morphological features define pre-organoids, spheroids were sorted into isolated groups based upon morphological features. Several methods exist for manipulating and isolating populations of single cells, but none are readily adaptable for sorting cell aggregates by an arbitrary feature set. Fluorescence-activated cell sorting (FACS) is high-throughput, fast and minimally damaging to the cells (Kovarik and Allbritton, 2011); however, it cannot sort on an arbitrary set of morphological
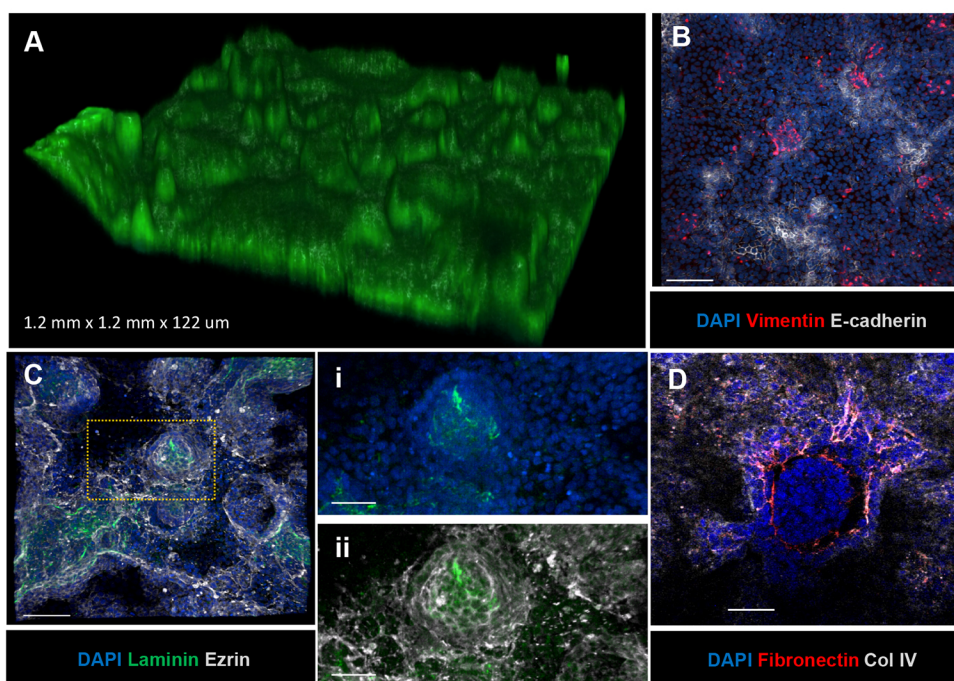

Fig. 2. Hindgut culture characterization. (A) Phalloidin (green) staining of hindgut cultures for F-actin illustrates the global 3D morphology over a 1.2 mm×1.2 mm region of the culture surface. (B) Hindgut cultures stained for the epithelial marker E-cadherin (white) and mesenchymal marker vimentin (red). (C) Hindgut cultures co-stained for nuclei (DAPI, blue), the epithelial cytoplasmic membrane protein ezrin (white), and basement membrane protein laminin (green). Insets show high-resolution images of the budding spheroid region co-stained for (i) DAPI and laminin and (ii) ezrin and laminin, to illustrate spatial organization within the bud. (D) Immunostaining for fibronectin (red) and collagen IV (Col IV, white). Scale bars: 100 µm in B,C,D; 50 µm in Ci,ii.

1.2 mm x 1.2 mm x 122 um

DAPI **Vimentin** E-cadherin

DAPI **Laminin** Ezrin

DAPI **Fibronectin** Col IV

features (Kovarik and Allbritton, 2011). Alternatively, traditional optical tweezers enable the manipulation within a dish, but not the isolation out of a dish of cell aggregates (Zhang and Liu, 2008; Hu and Sun, 2011). Micropipette-based sorting allows the isolation of cell aggregates based upon an arbitrary set of morphological features while having minimal isolation disturbance to neighboring aggregates (Anis et al., 2010). It is particularly powerful when combined with live-cell microscopy as it offers high spatiotemporal resolution, meaning it tracks the biophysical characteristics of a cell aggregate over both space and time. However, micropipette-based sorting is low-throughput as the capillary must be manually aligned with each target. Additionally, the isolation speed (time between when a cell aggregate is targeted and when it is dispensed) is slow, potentially exposing sensitive cells to activation of apoptotic signaling pathways (Portt et al., 2011).

Automated capillary-based sorting overcomes the low-throughput and slow isolation speed associated with capillary-based manual sorting while retaining the high spatiotemporal resolution and minimal isolation disturbance. Together, these features make automated capillary-based sorting appealing for searching for morphological features that distinguish pre-organoids from the bulk spheroid population.

Although progress has been made toward automating the collection of single cells, these systems are limited in capability and could not be applied to this problem (Hu and Sun, 2011; Wang et al., 2016). We thus custom-built an automated capillary-based sorting system that retains the advantages of those systems while bypassing their shortcomings. Our system consists of three major units: an image processing and analysis unit, a three-axis positioning unit, and a spheroid harvesting unit (Fig. 3A). The system can be replicated for relatively low cost from off-the-shelf
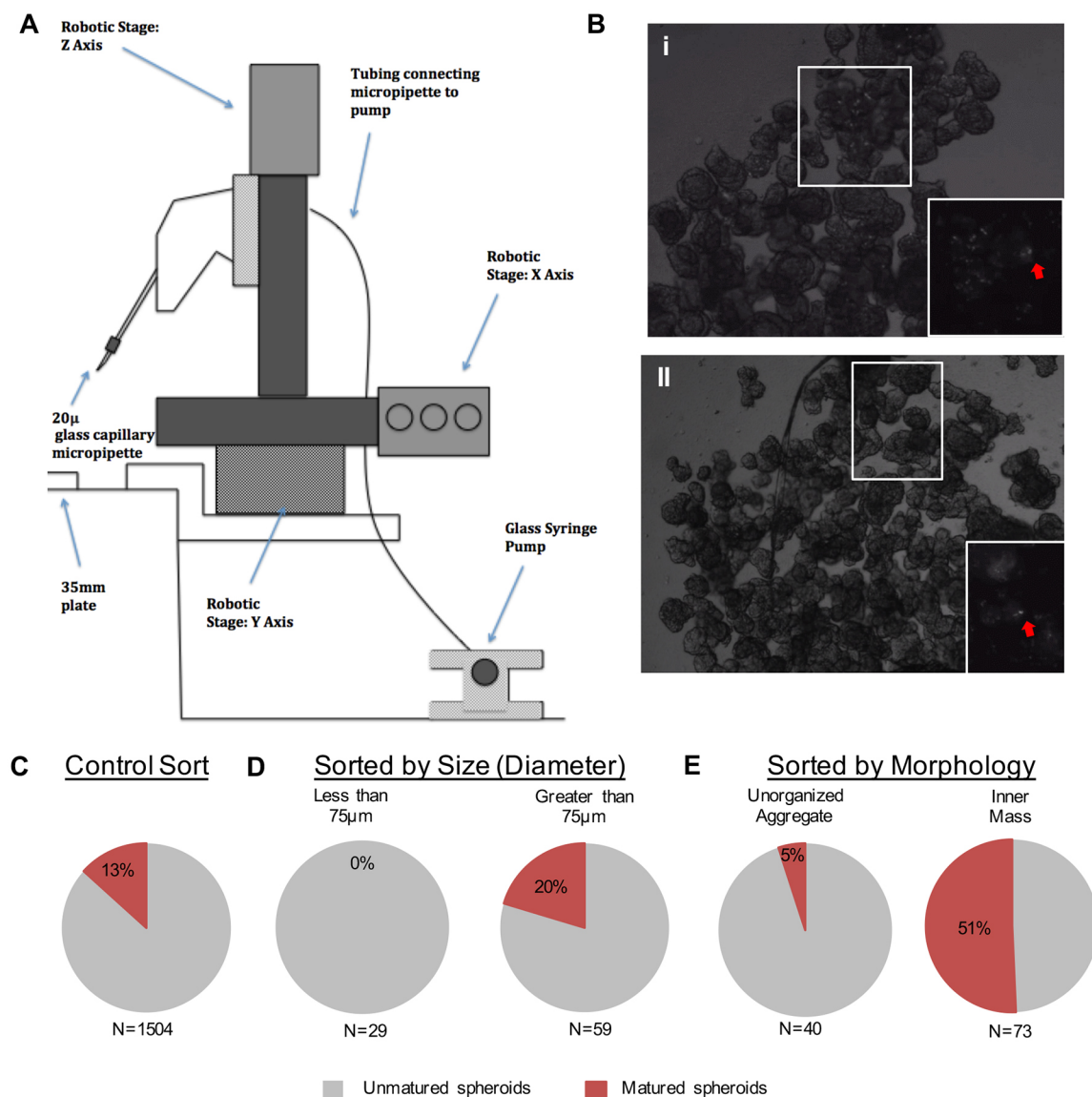

Fig. 3. Spheroid sorting. (A) System overview, three-axis positioning unit schematic. (B) Propidium iodide staining to mark dead cells in spheroids; (i) harvested spheroids, (ii) non-harvested spheroids. The red arrows indicate dead cells. Insets show magnification of marked regions. (C-E) Spheroids from hindgut induction days 5-8 went through the sorting process but were not separated by any parameters (C), were sorted by diameter (D), or were sorted by the morphological feature of an inner mass with an outer ring (E). The percentage in each pie chart is the percent of matured spheroids. The number below each pie graph indicates the total number of spheroids sorted for that condition.

components as a custom build to fit almost any existing microscope. The image processing and analysis unit takes as input a series of real-time images from the microscope and analyzes them for spheroids of interest. When a spheroid of interest is located, the image processing unit directs the three-axis positioning unit to move a micropipette into place. Finally, the spheroid harvesting unit takes up a single spheroid while minimally affecting the neighboring spheroids and holds it until all the collected spheroids are dispensed. Identifying and harvesting an individual spheroid takes only a few seconds, but when including the overhead time and time it takes to locate the next spheroid of interest, our sorting speed was ~1 spheroid min^{-1}.

Spheroids viable post-sorting

We verified that harvesting does no apparent harm in the short term (i.e. spheroids do not die during the sorting process) as indicated by propidium iodide staining of non-harvested spheroids and harvested spheroids immediately post-sorting (Fig. 3B). In order to establish that the harvesting process had no effect on long-term growth, maturation percentages were compared between spheroids that were harvested at random and unharvested spheroids (Table S1). After applying a Chi-squared test with Yates correction to the contingency table, a P-value of 0.417 was obtained, indicating that the harvesting process does not influence the maturation percentage.

Populations enriched for pre-organoids

In our hands, from an unsorted population of spheroids, only 13% are pre-organoids (Fig. 3C). Spheroids that do not mature into organoids either have stagnant growth or die (Fig. S3A), with the fate of the spheroid evident even 24 h after plating (Fig. S3B). When sorted by size with a diameter threshold of 75 μm, 0% of the spheroids with a diameter below 75 μm matured, suggesting that pre-organoids have a minimum size threshold. From the population with a diameter greater than 75 μm, 20% were pre-organoids, i.e. sorting by size enriches for pre-organoids by 1.5-fold (Fig. 3D). A P-value of 0.0056 from Boschloo's test indicates this finding is statistically significant. Sorting by the morphological feature of an inner mass yielded an even higher enrichment in pre-organoids in comparison with sorting by diameter. When a spheroid was positively identified with an inner mass, the likelihood of successful maturation into an intestinal organoid increased to 51%, which is a 3.8-fold enrichment over unsorted spheroids (Fig. 3E). A P-value of 0.00001 from Boschloo's test indicates this finding is statistically significant. Sorting by the size of the inner mass is unlikely to increase the pre-organoid enrichment as its diameter positively correlates with the diameter of the spheroid as a whole (Fig. S2C). Collectively, our data show that pre-organoid populations are generally spheroids with an inner mass, and a diameter larger than 75 μm.

We next determined if the spatial organization or the relative abundance of epithelial and mesenchymal cells was predictive of pre-organoid fate. We observed that spheroids emerge with different organization of the two cell types depending on the molecule used

to activate the Wnt pathway in the hindgut cultures, and both types of spheroids mature (Fig. S4). Additionally, we analyzed spheroid features associated with these two parameters on live spheroids stained for E-cadherin. The stain did not affect spheroid maturation (Table S2). Confocal images of 64 nascent spheroids, of which 16 were pre-organoids, were segmented, and nine features were selected for analysis. The first, a ratio of the volume of E-cadherin signal to the total volume of the spheroid, serves as a proxy for measuring the ratio of the two cell types within the spheroid. The remaining eight features serve to describe the spatial organization of the cell types within the spheroid. They are, briefly, the number of distinct Alexa Fluor 488-positive (green) regions; the second, third and fourth central moments of the centroids of the segmented green regions; the second, third and fourth central moments of the centroids of the green regions and the brightfield area centroid; and the mean Euclidean distance from each green centroid to the brightfield centroid. For each feature, the pre-organoids were compared with the rest of the spheroids using a two-sample t-test as shown in Table 1. From these data, we concluded that the ratio of the cell types is more important than their spatial organization in determining successful maturation, at least as measured by these features. Further details are provided in the Creation of the feature matrix section of the Materials and Methods.

DISCUSSION

We developed a workflow for identifying parameters that distinguish pre-organoids from other spheroids based on spheroid feature identification and automated analysis and collection. This process can be used to enrich for pre-organoids in the population of harvested spheroids. Our analysis revealed that the variability from the hindgut cultures carries over to the emergent spheroids and that spheroids successfully differentiating into pre-organoids have a minimum size and preferred morphology. The size threshold is likely indicative of the minimum number of cells needed for spheroids to emerge with the necessary relative amount of both epithelial and mesenchymal cells. This hypothesis follows from the fact that: (1) there is a minimum size threshold at which differentiation becomes favorable, and (2) the level of specialization in multicellular structures increases with the size of the system (Willensdorfer, 2008). Therefore, these features likely correlate with the expression of certain molecular markers in the spheroid and are indicators of the spheroid's underlying developmental trajectory. The morphology with an inner mesenchyme cell mass and outer ring of epithelial cells is a consequence of the budding process and frequently results in spheroids with the required ratio of both cell types.

Although the spheroid features that we sorted by – size and morphology – are both structural and therefore simple to sort for as they only require brightfield microscopy, our system can also sort by molecular markers if the spheroids have a fluorescent readout through an integrated reporter or a temporary dye. Furthermore, whereas we have focused solely on hPSC-derived hindgut organoids, and our reported parameters are specific to this system, the workflow, including identifying heterogeneous structural

Table 1. Spheroid features and their respective P-values as computed using a two-sample t-test

	Ratio*			Spatial organization‡					
Features	1	2	3	4	5	6	7	8	9
P-values	0.045	0.786	0.266	0.188	0.402	0.239	0.206	0.111	0.866

*Feature 1: Ratio of epithelial to mesenchymal cells.
‡Features 2-9: Spatial organization of epithelial and mesenchymal cells within the spheroid.

parameters and sorting based upon these, are easily generalizable to other organoid or aggregate systems.

Spheroid size and morphology likely have biological significance and are the focus of future mechanistic studies to fully understand how these parameters relate to the emergence of pre-organoid versus spheroid structures from hindgut cultures. We hypothesize that the mechanisms that govern the emergence of spheroids with an inner mass might be similar to those at play in the formation of the inner cell mass in the blastocyst (Piotrowska-Nitsche et al., 2005; Rossant, 2016). From our analysis of the 3D hindgut cultures and emergent spheroids, we can speculate as to how spheroids emerge and why the population is heterogeneous. Cells that differentiate into epithelial cells preferentially lie on top of the mesenchyme. As the cells proliferate and the cultures become overly confluent, bulging structures of varying sizes form with epithelial cells encapsulating underlying piles of mesenchymal cells. We observed no correlation between proliferation and budding regions (data not shown). These bulges progress to buds and detach from the cultures as spheroids. Production of a spheroid with both mesenchymal and epithelial cells requires coordinate detachment of the mesenchymal mass with the epithelia. Not all budding regions foster simultaneous detachment of connected epithelia and mesenchyme, giving rise to spheroids of heterogeneous composition and structure.

Isolating pre-organoids from the heterogeneous spheroid cultures offers multiple benefits in regards to downstream applications. Most importantly, downstream assays will be performed on a more homogeneous population, which will make the data easier to interpret and reproduce. Additionally, there are large cost savings in first enriching the spheroid population for pre-organoids because it obviates both the need to scale-up downstream, and to use potentially more involved assays to obtain the desired throughput. An even more efficient system would have a higher yield of pre-organoids from the initial differentiation and thus a more homogeneous spheroid population. To achieve this, we are studying the biomechanical forces that give rise to pre-organoids and applying our findings to reverse engineer the hindgut differentiation system, with the goal of exclusively producing pre-organoids.

MATERIALS AND METHODS
Differentiation into hindgut and spheroid maturation
Human pluripotent stem cells (hPSCs) (H1 from WiCell and hiPS72_3 generated by the Pluripotent Stem Cell Facility at Cincinnati Children's Hospital Medical Center) were maintained on hES Qualified Matrigel (BD Biosciences) in mTeSR1 medium (STEMCELL Technologies). The cells were passaged as colonies with dispase (1 mg ml^{-1}; Invitrogen) every 4 days. For differentiation, hPSC colonies were dissociated to single cells with StemPro Accutase (Invitrogen) and plated at 75,000 cells cm^{-2} in Matrigel-coated plates in mTeSR supplemented with Y-27632 (10 µM; Tocris). Exposure to ActivinA (100 ng ml^{-1}; Cell Guidance Systems) (Green and Smith, 1990) and increasing fetal bovine serum up to 2% (Hyclone) over the next 3 days directed the cells to form definitive endoderm. Subsequent exposure to FGF4 (500 ng ml^{-1}; Cell Guidance Systems) and CHIR99021 (3 µM; StemGent) for 5-8 days guided the cells to a hindgut fate (Dessimoz et al., 2006; McLin et al., 2007; Sherwood et al., 2011; Wells and Melton, 2000; Watson et al., 2014). CHIR99021 can be replaced with WNT3A (500 ng ml^{-1}; R&D Systems). Spheroids began budding off from the culture surface at D5. From D5 to D8 of hindgut culture, free-floating spheroids were collected daily. This differs from D3 to D4 in previous reports (Fig. S1). Collected spheroids, sorted or unsorted, settled to the bottom of a tube and then the medium was carefully removed. Matrigel (BD Biosciences, 354234) was gently mixed with the spheroids such that the spheroid concentration was less than 30 spheroids 50 µl^{-1} and

plated as 50 µl droplets. Spheroids embedded in Matrigel droplets were cultured in medium containing N2 supplement (1×; Invitrogen), B27 supplement (1×; Invitrogen), and EGF (50 ng ml^{-1}; R&D Systems) (Spence et al., 2011; McCracken et al., 2011). Sorted spheroids were counted after 10 days.

Sorting system
Physical system components
An Olympus IX81 microscope (Olympus) was fitted with a Hamamatsu C10600-0B-H microscope camera (Hamamatsu Photonics). The images were taken with a 4× objective and brightfield illumination, passed to a Dell Inspiron 3847 computer, and processed with MATLAB (MathWorks). The three-axis positioning unit, a schematic of which is shown in (Fig. 3A), allows the positioning of the micropipette near the spheroid of choice. It consists of three Zaber T-LSM025A motorized stages (Zaber Technologies, Vancouver, BC, Canada) arranged in an *x-y-z* configuration. The Zaber T-LSM025A motorized stages were controlled through commands sent over a serial port via a modified MATLAB library developed by Dominik Hofer (MathWorks File Exchange, 2013; https://www. mathworks.com/matlabcentral/fileexchange/40197-zaber-t-lsm-translation-stage-driver). The three-axis positioning unit was mounted onto the side of an Olympus IX2-SP stage (Olympus) through custom 3D-printed parts. In total, the system measures 134 mm×156 mm×186 mm, not including the harvesting unit. The spheroid harvesting unit consists of another Zaber T-SM025A stage. A 250 µl Hamilton Syringe (Model 1725 TLL SYR, Hamilton Company) was attached to the Zaber actuator, with custom 3D-printed parts. The Zaber actuator can achieve speeds from 0.0022 mm sec^{-1} to 7 mm sec^{-1}. The micropipette tips can range from sub-micron to 300 µm. Using rough calculations (neglecting any drag), the pump can achieve flow velocities at the tip of the micropipette ranging from ∼1 nl sec^{-1} to 500 nl sec^{-1} with a 150 µm tip. As with the three-axis positioning unit, the syringe pump is quite compact with dimensions of 148 mm×66 mm×52 mm. The syringe pump was connected to an Eppendorf Universal Capillary Holder (Eppendorf) through one-quarter inch tubing (Eppendorf) and the required adaptors (Connectors P-680 and P-720, Idex Health and Science, Middleborough, MA, USA). Finally, the Universal Capillary Holder held a micropipette (G150TF-4, Warner Instruments, Hamden, CT, USA) that was pulled with a P-97 micropipette puller (Sutter Instrument, San Francisco, CA, USA).

Segmentation
The first step toward sorting required that the spheroids be segmented from the background of the microscope images. Under brightfield illumination, the suspended spheroids stand out from the background. To detect this, the Canny Edge Detection Algorithm was applied. This provided clusters of edges that were connected by morphologically dilating and filling the image. The connected regions were then morphologically opened to remove thin segments, and the entire image was de-noised by removing any connected regions with a pixel area smaller than a threshold. Finally, any connected region touching the border of the image was also removed as it complicated classification. A condensed version of the algorithm is shown in Fig. S5. After segmentation, properties of each connected region, including location, area, perimeter, major and minor axis lengths, and eccentricity, were identified (Fig. S5D).

Classification
Spheroids were then classified separately by two morphological features: a diameter threshold of 75 µm and by the presence of an inner mass (Fig. 1A,F). In order to classify by diameter, the major and minor axis of each connected region, as visualized in a planar image, were averaged. As the connected regions are not necessarily ellipses, the major and minor axis were found on an ellipse that had the same second central moments as the connected region in question. Classification for spheroids with an inner mass, which vary highly in physical appearance as illustrated in Fig. 1A, was achieved by a semi-autonomous classification system where the user made the final judgment (Fig. S6). The image processing and analysis unit extracted a local binary pattern (LBP) feature vector from the segmented microscope image and passed it to a pre-trained support vector machine

(SVM) classifier (Ojala et al., 2002). The user then confirmed if the spheroid had an inner mass. As a result, the classification for presence of an inner mass was made reliably with the user in the loop. After classification, the micropipette was moved into place by the three-axis positioning unit, which was constructed as shown in Fig. 3A.

Harvesting

The collected spheroids were suspended in 4 ml of Advanced DMEM/F12 media (Thermo Fisher Scientific) in a 35 mm Falcon cell culture dish (Corning) and allowed to settle for 5 min in an incubator. Concurrently, the fluidics system was flooded with DMEM media, with extra care taken to eliminate air bubbles. The spheroids were taken from the incubator and observed with the 4× objective and brightfield illumination. Target spheroids were identified with the segmentation and classification algorithms written in MATLAB. The spheroids were then chosen and harvested. MATLAB code was run to calibrate the position of the micropipette tip within the image. After collection the target spheroids were dispensed into a 2 ml Falcon tube with minimal spheroid loss (Corning) and subsequently plated for spheroid maturation.

Statistical test choice

A two-tailed Boschloo's test, which involves using the P-value for Fisher's test as the test statistic, was used as low sample numbers ruled out using the Chi-squared test and Boschloo's test has been shown to be uniformly more powerful than Fisher's exact test (Berger and Sidik, 2003). A confidence level of 0.05 was chosen.

Spatial organization versus ratio of cell types

Live spheroids were stained for E-cadherin, gently embedded in Matrigel, and subsequently imaged using a confocal microscope. The location of each imaged spheroid was noted, allowing imaging of the same spheroid after 10 days, at which point the spheroid was classified as pre-organoid or not.

Segmentation of confocal image stacks

The image stacks contained two channels, a brightfield channel and an Alexa Fluor 488 (green) channel. The Alexa Fluor 488 images tended to be noisy as the E-cadherin stain was faint. Thus, the first step to segmenting was to de-noise the image by performing a morphological opening. Next, the image was thresholded with Otsu's method (Otsu, 2007). Finally, a morphological closing of the image was performed to eliminate thin components. A sample segmentation is shown in Fig. S7A. The brightfield images were more challenging as out-of-plane light contributes to each slice in the form of blurred portions of the image. Thus, the first step was to take the magnitude of the spatial gradient in x and y. This eliminated some, but not all, of the blurred regions. Next, Canny Edge Detection was used to identify clusters of edges. These were connected by morphologically dilating and filling the image. Finally, noise was eliminated by removing any connected region with a pixel area smaller than a threshold. A sample segmentation is shown in Fig. 7B.

Creation of the feature matrix

The goal of this experiment is to determine whether either the spatial organization or the ratio of the epithelium and mesenchyme within a spheroid is a good predictor of it being a pre-organoid. Nine features were tested, with the first designed to test the importance of the ratio of the cell types and the remaining eight designed to test the importance of the spatial organization.

The first feature is:

$$F_1 = \frac{\text{Volume}_{\text{green}}}{\text{Volume}_{\text{brightfield}}}.$$

This serves as a proxy for the percentage of epithelial cells within a spheroid and thus a measure of the ratio of the two cell types within a spheroid.

The second feature is the number of green regions. A green region is defined as the set of pixels that are spatially touching. Fig. S7C shows a spheroid that has two green regions. This can physically be interpreted as whether the epithelial cells tend to group together into one distinct group or tend to form smaller clusters.

In order to further test the importance of the spatial organization of the cell types, two matrices were constructed. First, the centroids of all the green regions were assembled into a $F_2 \times 3$ matrix C_{green}, where F_2 is the number of green regions as described above. Similarly, a $(F_2+1) \times 3$ matrix C was constructed by adding the brightfield regions centroid to the bottom of the C_{green} matrix. All centroids were scaled to µm from pixels.

The third, fourth and fifth features are the means of the second, third and fourth central moments taken along the columns of the C_{green} matrix respectively. The second central moment, also called the variance, is a measure how far the centroids are spread from their mean. The third central moment, also called the skewness, is a measure of asymmetry of the distribution of the centroids. The fourth central moment, also called the kurtosis, is a measure of how outlier-prone the distribution of the centroids. As the spheroids are not expected to be asymmetric about the arbitrarily defined axes, the mean of each of the central moments was taken. Similarly, the sixth, seventh and eighth features were the second, third, and fourth central moments of the C matrix, respectively.

The ninth feature was the mean Euclidean distance between each green centroid and the brightfield centroid. For each spheroid, all nine features were found and the spheroid was grouped into one of two classes, pre-organoid or not, depending on whether it had successfully matured.

For each feature, a two-sample t-test was used to compare the pre-organoids and the rest of the spheroids. The results are summarized in Table 1.

Testing spheroid viability

Harvested and non-harvested spheroids were stained with propidium iodide for 10 min at 37°C to identify dead cells. Both groups were imaged and the amount of fluorescence was quantified.

Immunohistochemistry and microscopy

Spheroids for live staining were collected and let settle by gravity. Primary antibody against E-cadherin (AF648, R&D Systems, 1:50) was added to PBS containing 5% donkey serum. Samples were stained at 37°C for 1.5 h and then washed with PBS. The samples were exposed to secondary antibody donkey anti-goat Alexa Fluor 488 (A-11055, Life Technologies, 1:400) in PBS with 5% donkey serum for 1 h at 37°C and then washed with PBS. Hindgut cultures or nascent spheroids were fixed in 4% paraformaldehyde at room temperature for 15 min. Samples were treated with 0.25% Triton X-100 in PBS for 10 min at room temperature, blocked in PBS with 10% donkey serum for 1 h at room temperature, and then stained in PBS with 5% donkey serum using a selection of the following primary antibodies overnight at 4°C: anti-human CDX-2 (CDX2-88, BioGenex Laboratories, 1:300-1:500), anti-laminin (ab11575, Abcam, 1:200), anti-collagen IV (ab6586, Abcam, 1:250), anti-fibronectin (CP70, Millipore, 1:100), anti-ezrin (3C12, Abcam, 1:500), anti-human vimentin (C-20, Santa Cruz Biotechnology, 1:50), and anti-human E-cadherin (AF648, R&D Systems, 1:50; 24E10, Cell Signaling Technology, 1:500; ab15148, Abcam, 1:500). The following secondary antibodies in PBS with 5% donkey serum were incubated with the samples at room temperature for 2 h: donkey anti-goat Alexa Fluor 488 (A-11055, Life Technologies, 1:750), donkey anti-mouse Alexa Fluor 568 (A-10037, Life Technologies, 1:500), donkey anti-rat Alexa Fluor 647 (712-605-153, Jackson ImmunoResearch, 1:500), and donkey anti-rabbit Alexa Fluor 568 (ab175470, Abcam, 1:500). DAPI was used as a nuclear stain. Hindgut cultures were mounted with Vectashield Mounting Medium (Vector Laboratories); nascent spheroids were mounted in 50% Aqua-Poly/Mount (Polyscience) on glass slides, using 0.2 mm-deep iSpacers from the SunJin Lab (http://www.sunjinlab.com/) to prevent spheroid deformation.

Imaging was performed on a Nikon A1 confocal microscope, using either a 100× or 60×/1.3 NA oil objective. z-stacks (500 nm steps) of mounted spheroids were acquired using the 405 nm diode laser, 561 nm diode-pumped solid-state (DPSS) laser, a 638 nm diode laser, as well as a 488 nm argon gas laser line. The data were viewed and processed in Imaris (Bitplane), using the software's built-in tools. For cell counting, the datasets (z-stacks of spheroids stained with DAPI) are first rendered in 3D, and using

the Spots function, Imaris detects an automatic threshold to insert the spots. The DAPI channel and the spots were simultaneously visualized, allowing the threshold to be adjusted manually. The number and positions of the detected spots were retrievable under the Statistics tab.

References

Anis, Y. H., Holl, M. R. and Meldrum, D. R. (2010). Automated selection and placement of single cells using vision-based feedback control. IEEE Trans. Automat. Sci. Eng. 7, 598-606.

Berger, R. L. and Sidik, K. (2003). Exact unconditional tests for a 2×2 matched-pairs design. Stat. Methods Med. Res. 12, 91-108.

Boehnke, K., Iversen, P. W., Schumacher, D., Lallena, M. J., Haro, R., Amat, J., Haybaeck, J., Liebs, S., Lange, M., Schafer, R. et al. (2016). Assay establishment and validation of a high-throughput screening platform for three-dimensional patient-derived colon cancer organoid cultures. J. Biomol. Screen. 21, 931-941.

Dessimoz, J., Opoka, R., Kordich, J. J., Grapin-Botton, A. and Wells, J. M. (2006). FGF signaling is necessary for establishing gut tube domains along the anterior-posterior axis in vivo. Mech. Dev. 123, 42-55.

Edmondson, R., Broglie, J. J., Adcock, A. F. and Yang, L. (2014). Three-dimensional cell culture systems and their applications in drug discovery and cell-based biosensors. Assay Drug Dev. Technol. 12, 207-218.

Eglen, R. M. and Randle, D. H. (2015). Drug discovery goes three-dimensional: goodbye to flat high-throughput screening? Assay Drug Dev. Technol. 13, 262-265.

Gordon, S., Daneshian, M., Bouwstra, J., Caloni, F., Constant, S., Davies, D. E., Dandekar, G., Guzman, C. A., Fabian, E., Haltner, E. et al. (2015). Non-animal models of epithelial barriers (skin, intestine and lung) in research, industrial applications and regulatory toxicology. Altex 32, 327-378.

Green, J. B. A. and Smith, J. C. (1990). Graded changes in dose of a Xenopus activin A homologue elicit stepwise transitions in embryonic cell fate. Nature 347, 391-394.

Hu, S. and Sun, D. (2011). Automatic transportation of biological cells with robot-tweezer manipulation system. Int. J. Rob. Res. 30, 1681-1694.

Kovarik, M. L. and Allbritton, N. L. (2011). Measuring enzyme activity in single cells. Trends Biotechnol. 29, 222-230.

Lancaster, M. A. and Knoblich, J. A. (2014). Organogenesis in a dish: modeling development and disease using organoid technologies. Science 345, 1247125.

Lancaster, M. A., Renner, M., Martin, C.-A., Wenzel, D., Bicknell, L. S., Hurles, M. E., Homfray, T., Penninger, J. M., Jackson, A. P. and Knoblich, J. A. (2013). Cerebral organoids model human brain development and microcephaly. Nature 501, 373-379.

Liu, S., Zhang, D., Chen, Y., Wang, B. and Qiao, L. (2015). Potential applications of induced pluripotent stem cells (iPSCs) in the modeling of gastrointestinal disorders. Curr. Stem Cell Res. Ther. 10, 220-227.

Matano, M., Date, S., Shimokawa, M., Takano, A., Fujii, M., Ohta, Y., Watanabe, T., Kanai, T. and Sato, T. (2015). Modeling colorectal cancer using CRISPR-Cas9-mediated engineering of human intestinal organoids. Nat. Med. 21, 256-262.

Matthys, O. B., Hookway, T. A. and McDevitt, T. C. (2016). Design principles for engineering of tissues from human pluripotent stem cells. Curr. Stem Cell Rep. 2, 43-51.

McCracken, K. W., Howell, J. C., Wells, J. M. and Spence, J. R. (2011). Generating human intestinal tissue from pluripotent stem cells in vitro. Nat. Protoc. 6, 1920-1928.

McCracken, K. W., Catá, E. M., Crawford, C. M., Sinagoga, K. L., Schumacher, M., Rockich, B. E., Tsai, Y.-H., Mayhew, C. N., Spence, J. R., Zavros, Y. et al. (2014). Modelling human development and disease in pluripotent stem-cell-derived gastric organoids. Nature 516, 400-404.

McDonald, A. C. H. and Rossant, J. (2014). Gut endoderm takes flight from the wings of mesoderm. Nat. Cell Biol. 16, 1128-1129.

McLin, V. A., Rankin, S. A. and Zorn, A. M. (2007). Repression of Wnt/beta-catenin signaling in the anterior endoderm is essential for liver and pancreas development. Development 134, 2207-2217.

Ojala, T., Pietikainen, M. and Maenpaa, T. (2002). Multiresolution gray-scale and rotation invariant texture classification with local binary patterns. IEEE Trans. Pattern Anal. Mach. Intell. 24, 971-987.

Otsu, N. (2007). A threshold selection method from gray-level histograms. IEEE Transactions on Systems, Man, and Cybernetics 9, 62-66. http://ieeexplore.ieee.org/document/4310076.

Piotrowska-Nitsche, K., Perea-Gomez, A., Haraguchi, S. and Zernicka-Goetz, M. (2005). Four-cell stage mouse blastomeres have different developmental properties. Development 132, 479-490.

Portt, L., Norman, G., Clapp, C., Greenwood, M. and Greenwood, M. T. (2011). Anti-apoptosis and cell survival: a review. Biochim. Biophys. Acta 1813, 238-259.

Purpura, K. A., Bratt-Leal, A. M., Hammersmith, K. A., McDevitt, T. C. and Zandstra, P. W. (2012). Systematic engineering of 3D pluripotent stem cell niches to guide blood development. Biomaterials 33, 1271-1280.

Rossant, J. (2016). Making the mouse blastocyst: past, present, and future. Curr. Top. Dev. Biol. 117, 275-288.

Rubin, D. C. (2007). Intestinal morphogenesis. Curr. Opin. Gastroenterol. 23, 111-114.

Sherwood, R. I., Maehr, R., Mazzoni, E. O. and Melton, D. A. (2011). Wnt signaling specifies and patterns intestinal endoderm. Mech. Dev. 128, 387-400.

Si-Tayeb, K., Noto, F. K., Nagaoka, M., Li, J., Battle, M. A., Duris, C., North, P. E., Dalton, S. and Duncan, S. A. (2010). Highly efficient generation of human hepatocyte-like cells from induced pluripotent stem cells. Hepatology 51, 297-305.

Sinagoga, K. L. and Wells, J. M. (2015). Generating human intestinal tissues from pluripotent stem cells to study development and disease. EMBO J. 34, 1149-1163.

Spence, J. R., Mayhew, C. N., Rankin, S. A., Kuhar, M. F., Vallance, J. E., Tolle, K., Hoskins, E. E., Kalinichenko, V. V., Wells, S. I., Zorn, A. M. et al. (2011). Directed differentiation of human pluripotent stem cells into intestinal tissue in vitro. Nature 470, 105-109.

Sun, D., Lennernas, H., Welage, L. S., Barnett, J. L., Landowski, C. P., Foster, D., Fleisher, D., Lee, K. D. and Amidon, G. L. (2002). Comparison of human duodenum and Caco-2 gene expression profiles for 12,000 gene sequences tags and correlation with permeability of 26 drugs. Pharm. Res. 19, 1400-1416.

Świerczek, B., Ciemerych, M. A. and Archacka, K. (2015). From pluripotency to myogenesis: a multistep process in the dish. J. Muscle Res. Cell Motil. 36, 363-375.

Takasato, M., Er, P. X., Becroft, M., Vanslambrouck, J. M., Stanley, E. G., Elefanty, A. G. and Little, M. H. (2014). Directing human embryonic stem cell differentiation towards a renal lineage generates a self-organizing kidney. Nat. Cell Biol. 16, 118-126.

Takebe, T., Sekine, K., Enomura, M., Koike, H., Kimura, M., Ogaeri, T., Zhang, R.-R., Ueno, Y., Zheng, Y.-W., Koike, N. et al. (2013). Vascularized and functional human liver from an iPSC-derived organ bud transplant. Nature 499, 481-484.

Tian, L., Deshmukh, A., Ye, Z. and Jang, Y.-Y. (2016). Efficient and controlled generation of 2D and 3D bile duct tissue from human pluripotent stem cell-derived spheroids. Stem Cell Rev. 12, 500-508.

Wang, Z., Feng, C., Muruganandam, R., Mathew, J., Wong, P. C., Ang, W. T., Tan, S. Y. M. and Latt, W. T. (2016). A fully automated robotic system for three-dimensional cell rotation. Proceedings of 2016 IEEE International Conference on Robotics and Automation (ICRA), pp. 1707-1712, Stockholm, Sweden.

Watson, C. L., Mahe, M. M., Múnera, J., Howell, J. C., Sundaram, N., Poling, H. M., Schweitzer, J. I., Vallance, J. E., Mayhew, C. N., Sun, Y. et al. (2014). An in vivo model of human small intestine using pluripotent stem cells. Nat. Med. 20, 1310-1314.

Wells, J. M. and Melton, D. A. (2000). Early mouse endoderm is patterned by soluble factors from adjacent germ layers. Development 127, 1563-1572.

Willensdorfer, M. (2008). Organism size promotes the evolution of specialized cells in multicellular digital organisms. J. Evol. Biol. 21, 104-110.

DEVELOPMENT

Yang, L., Geng, Z., Nickel, T., Johnson, C., Gao, L., Dutton, J., Hou, C. and Zhang, J. (2016). Differentiation of human induced-pluripotent stem cells into smooth-muscle cells: two novel protocols. *PLoS ONE* **11**, e0147155.

Zahabi, A., Shahbazi, E., Ahmadieh, H., Hassani, S.-N., Totonchi, M., Taei, A., Masoudi, N., Ebrahimi, M., Aghdami, N., Seifinejad, A. et al. (2012). A new efficient protocol for directed differentiation of retinal pigmented epithelial cells from normal and retinal disease induced pluripotent stem cells. *Stem Cells Dev.* **21**, 2262-2272.

Zhang, H. and Liu, K.-K. (2008). Optical tweezers for single cells. *J. R. Soc. Interface* **5**, 671-690.

Zhang, J., Klos, M., Wilson, G. F., Herman, A. M., Lian, X., Raval, K. K., Barron, M. R., Hou, L., Soerens, A. G., Yu, J. et al. (2012). Extracellular matrix promotes highly efficient cardiac differentiation of human pluripotent stem cells: the matrix sandwich method. *Circ. Res.* **111**, 1125-1136.

Zhao, Y. H., Le, J., Abraham, M. H., Hersey, A., Eddershaw, P. J., Luscombe, C. N., Boutina, D., Beck, G., Sherborne, B., Cooper, I. et al. (2001). Evaluation of human intestinal absorption data and subsequent derivation of a quantitative structure-activity relationship (QSAR) with the Abraham descriptors. *J. Pharm. Sci.* **90**, 749-784.

DEVELOPMENT